

Computational Fermi level engineering and doping-type conversion of Ga₂O₃ via three-step synthesis process

Anuj Goyal¹, Andriy Zakutayev¹, Vladan Stevanović^{1,2}, Stephan Lany¹

¹National Renewable Energy Laboratory, Golden, CO, 80401, United States.

²Colorado School of Mines, Golden, CO, 80401, United States

Abstract

Ga₂O₃ is being actively explored for high-power and high-temperature electronics, deep-ultraviolet optoelectronics, and other applications due to its ultra-wide bandgap and low projected fabrication cost of large-size and high-quality crystals. Efficient *n*-type doping of Ga₂O₃ has been achieved, but *p*-type doping faces fundamental obstacles due to compensation, deep acceptor levels, and the polaron transport mechanism of free holes. However, aside from achieving *p*-type conductivity, plenty of opportunity exists to engineer the position of the Fermi level for improved design of Ga₂O₃ based devices. We use first-principles defect theory and defect equilibrium calculations to simulate a 3-step growth-annealing-quench synthesis protocol for hydrogen assisted Mg doping in β-Ga₂O₃, taking into account the gas phase equilibrium between H₂, O₂ and H₂O, which determines the H chemical potential. We predict Ga₂O₃ doping-type conversion to a net *p*-type regime after growth under reducing conditions in the presence of H₂ followed by O-rich annealing, which is a similar process to the Mg acceptor activation by H removal in GaN. For equilibrium annealing with re-equilibration of compensating O vacancies, there is an optimal temperature that maximizes the Ga₂O₃ net acceptor density for a given Mg doping level, which is further increased in the non-equilibrium annealing scenario without re-equilibration. After quenching to operating temperature, the Ga₂O₃ Fermi level drops below mid-gap down to about +1.5 eV above the valence band maximum, creating a significant number of uncompensated neutral Mg_{Ga}⁰ acceptors. The resulting free hole concentration in Ga₂O₃ is very low even at elevated operating temperature (~10⁸ cm⁻³ at 400C) due to deep energy level of these Mg acceptors, and hole conductivity is further impeded by the polaron hopping mechanism. However, the Fermi level reduction down to +1.5 eV and suppression of free electron density in this doping type converted (*N_A* > *N_D*) Ga₂O₃ material is of significance and impact for the design of Ga₂O₃ power electronics devices.

Monoclinic beta-phase of gallium oxide (β -Ga₂O₃) an exciting material for various (opto)electronic and energy-related technologies due to its ultra-wide bandgap (~4.9 eV) and the ability to grow large-size high-quality single crystals at low projected cost.^{1,2} Considered applications include various power electronic devices³, radio-frequency transistors^{4,5}, solar-blind photo-detectors⁶⁻⁸, gas sensors^{9,10}, contact layers in photovoltaics^{11,12}, and other applications^{13,14}. In power electronics, dedicated efforts in recent years towards improving crystal growth, *n*-type doping, and device fabrication led to substantial progress in performance of β -Ga₂O₃ based horizontal transistors, vertical Schottky barrier diodes (SBDs), vertical metal oxide semiconductor field effect transistors (MOSFETs), and related devices¹⁵⁻¹⁷. For example, depletion mode (normally-on) current aperture vertical β -Ga₂O₃ MOSFETs with implantation doping¹⁷ and enhancement-mode (normally-off) Ga₂O₃ vertical transistors with fin-shaped channels¹⁸ have been demonstrated. However, one of the biggest challenges in realizing the true potential of Ga₂O₃ in power electronics, along with its low thermal conductivity, is the absence of *p*-type doping, limiting the design of device structures that can be realized¹⁶.

Ga₂O₃ is intrinsically an *n*-type semiconductor. Using extrinsic donors its *n*-type conductivity is easily tunable over many orders of magnitude^{1,19-23}, but *p*-type doping faces fundamental obstacles²⁴⁻³¹. Among various acceptor dopants in Ga₂O₃, Mg is computationally predicted to be the most stable²⁷ and was also experimentally found to reduce the unintentional *n*-type conductivity and increase the resistivity of the material²⁶. Mg doped Ga₂O₃ has been synthesized³² and studied³³ using an electron paramagnetic resonance (EPR) technique, where Mg acceptor (0/1-) level is experimentally determined to be at $E_V+0.7$ eV. However, in a photoluminescence study³⁴, the Mg acceptor level is shown to be deeper at $E_V+1.0$ eV, which compares better with the theoretical predictions employing hybrid functional calculations^{25,28,35,36}, where (0/1-) level is estimated to be between $E_V+1.0$ to 1.5 eV. The differences in theoretical predictions published in literature originate to some extent from different fraction of exact (non-local) exchange employed in these hybrid functional calculations. In more recent computational work, focus has been towards studying diffusion²⁸, EPR³⁷ and luminescence properties³⁸ of Mg doped Ga₂O₃.

While the prospects of achieving *p*-type conductivity through acceptor doping in β -Ga₂O₃ remain bleak, ample opportunities exist for Fermi level engineering of Ga₂O₃ power electronic devices via acceptor-type dopants^{1,16,26}. Even when holes remain localized at the acceptor site or as small polarons, the doping can cause the acceptor concentration (N_A) to exceed the donor concentration (N_D). The result is a doping type conversion with a large drop of the Fermi level E_F where electrons become minority carriers. The resulting acceptor-doped Ga₂O₃ material can be used as buried electron barrier, a.k.a. current blocking layer, for controlling the turn-on voltage and saturation current of vertical metal-oxide-semiconductor field effect transistors (MOSFET) with current aperture. Such acceptor-doped Ga₂O₃ can be also used for increasing the breakdown voltage and decreasing the leakage current of vertical MOSFET and Schottky diodes using edge termination by guard rings and related structures^{1,16,17,26,39}. It is likely that such acceptor doped β -Ga₂O₃ can be achieved using non-equilibrium synthesis process with mobile hydrogen, species that was instrumental in achieving *p*-type doping of GaN, which led to the development of the blue light emitting diode.⁴⁰⁻⁴⁴ More recently, non-equilibrium processing involving hydrogen and oxygen was employed to reduce the electron density in otherwise degenerately doped ZnSnN₂^{45,46} and MgZrN₂.⁴⁷

Here we study H-assisted Mg doping of β -Ga₂O₃ under non-equilibrium growth and annealing process, in a broad analogy to the well-known strategies for activating *p*-type conductivity in Mg-doped GaN thin films, using first principles supercell calculations and thermodynamic defect equilibrium simulations. Although traditional *p*-type semiconductivity resulting from thermal ionization of free holes at room temperature in Ga₂O₃ remains beyond reach, we report quantitative computational predictions for synthesis process conditions that enable doping type conversion in Ga₂O₃. We predict doping-type conversion to a net *p*-type regime after O-rich annealing of Ga₂O₃ grown under reducing conditions in the presence of H₂. The resulting doping type-converted Ga₂O₃ has Fermi level +1.5 eV above the valence band maximum due to uncompensated neutral Mg_{Ga}⁰ acceptors, but the resulting free hole concentration is very low ($\sim 10^8$ cm⁻³ even at 400C) due to deep energy level of these acceptors. These theoretical predictions are expected to guide experimental tuning of growth and annealing conditions to achieve doping type converted Ga₂O₃ for realization of novel device configurations.

As illustrated in Figure 1, our approach consists of a three-step process of (1) thin-film growth under O-poor conditions in the presence of hydrogen, (2) acceptor activation via annealing in an O-rich/H-poor atmosphere, and (3) quenching to a range of operating temperatures. The thermodynamic simulations take into account the $\text{H}_2 + \frac{1}{2}\text{O}_2 \leftrightarrow \text{H}_2\text{O}$ gas phase equilibrium connecting the O and H chemical potentials. In the growth step, the presence of H donor impurities can increase the solubility of substitutional Mg_{Ga} acceptors, and it reduces the concentrations of compensating O vacancies (*V*_O) while the system remains *n*-type. In the annealing step, meant to purge the mobile H donor species, we consider two different stages of non-equilibrium. In the more readily realizable scenario, only the equilibration of the Mg solubility is suppressed. In the second scenario, which might be more difficult to realize, also the equilibration of *V*_O formation is suppressed, thereby allowing for maximal non-equilibrium activation of acceptor dopants and ensuing Fermi level reduction. In the quenching step, it is assumed that all dopant and defect concentrations remain at the level of the preceding process step, and only the Fermi level (*E*_F) and the corresponding electron and hole densities are equilibrated to the operating temperature of interest.

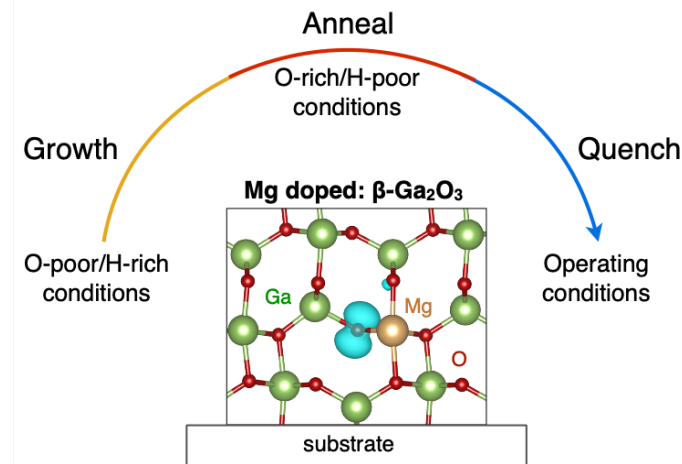


Figure 1. Schematic illustration of thermodynamic conditions in the modeling of growth, annealing, and quenching steps of Mg-doped β -Ga₂O₃. The atomic structure model shows

the spin-density iso-surface (blue) associated with the defect-bound hole-polaron created by the neutral Mg_{Ga}^0 acceptor at a neighboring O site.

Defect calculations. The stable phase, $\beta\text{-Ga}_2\text{O}_3$, has a monoclinic crystal structure (space group C2/m) with two non-equivalent crystallographic Ga sites (Ga1 tetrahedral, and Ga2 octahedrally coordinated) and three O sites (O1 bonded to one Ga1 and two Ga2, O2 bonded to two Ga1 and one Ga2, and O3 bonded to one Ga1 and three Ga2). Figure 1 shows the hole charge density of the Mg_{Ga} defect (from hybrid functional calculations) in the neutral charge state in the Ga_2O_3 crystal structure illustrating the “polaronic” deep nature of Mg_{Ga} acceptor defect level. Mg prefers the six-fold coordinated Ga2 site, and the acceptor-hole is localized on the neighboring O1 site. Our simulated description of Mg_{Ga} acceptor is consistent with the EPR study⁴⁸ that also found the hole to be located at the O1 nearest neighbor oxygen site.

We calculated the acceptor levels for the two Mg_{Ga} configurations using a hybrid functional (see below for computational details). The formation energies ΔH_b of dopants, defects, dopant-defect pairs and complexes were calculated using the approach of Ref⁴⁹, combining density functional theory (DFT) supercell energies with GW band gap corrections and fitted elemental reference energies⁵⁰ (FERE). We included the native defects (V_{Ga} , V_{O}), extrinsic dopants (Mg_{Ga} , Mg_i , H_i) and defect pairs and complexes ($\text{Mg}_{\text{Ga}}+V_{\text{O}}$, $2\text{Mg}_{\text{Ga}}+V_{\text{O}}$, $\text{Mg}_{\text{Ga}}+\text{H}_i$) expected to form due to charge compensation. H can also substitute for oxygen (H_O),²² but we find that the formation energy of H_O is 0.5 eV higher than that of H_i even under the extreme limit of O poor conditions ($\Delta\mu_{\text{Ga}} = 0$, $\Delta\mu_{\text{O}} = -3.75$ eV), and we will therefore not further consider H_O in this study.

Table 1 lists the defect formation energies and the binding energies ΔE_b of defect pairs, where the formation energies are given for the convention $E_F = E_{\text{VBM}}$ and $\Delta\mu_i = 0$, and the actual values of ΔH_b at any given point in the thermodynamic simulation (see below) are determined for the actual Fermi level position and chemical potentials.⁴⁹ The formation energy of the Mg_{Ga}^0 defect on the Ga2 site is lower by 0.43 eV compared to Mg substituting the Ga1 site, and the (0/1-) charge transition level is calculated at 1.0 and 1.1 eV above the valence band maximum (VBM) for Mg on the Ga2 and Ga1 site, respectively. Oxygen vacancies in Ga_2O_3 act as deep donors, with a (2+/0) charge transition ~ 1.3 eV below the conduction band minimum (CBM), whereas the hydrogen interstitial act as shallow donor, stable in the 1+ charge state throughout the range of Fermi energies in the bandgap, consistent with prior literature results.^{22,24} We find that the binding of the H interstitial to Mg acceptors is weaker than the binding of O vacancies (*cf.* Table 1), suggesting that H interstitials are more easily separated from the acceptors during annealing and activation than the O vacancies.

Table 1: Calculated formation energies ΔH_{ref} of defects and dopants and the binding energies ΔE_b of dopant-defect complexes. The formation energies are given for a reference condition (see Ref. 47), with the chemical potentials set to elemental reference ($\Delta\mu_i = 0$) and the Fermi energy set to the VBM.

Defect	ΔH_{ref} (eV)	Defect complex	ΔE_b (eV)
$V_{\text{O}1}^{2+}$	-2.53	$(\text{Mg}_{\text{Ga}2} + V_{\text{O}1})^+$	-0.74
$V_{\text{O}2}^{2+}$	-1.83	$(\text{Mg}_{\text{Ga}2} + V_{\text{O}2})^+$	-0.58
$V_{\text{O}3}^{2+}$	-2.66	$(\text{Mg}_{\text{Ga}2} + V_{\text{O}3})^+$	-0.62

$V_{\text{Ga}1}^{3-}$	+16.71	$(\text{Mg}_{\text{Ga}2} + \text{H}_i)^0$	-0.44
$\text{Mg}_{\text{Ga}2}^{1-}$	+2.12	$(2\text{Mg}_{\text{Ga}2} + V_{\text{O}1})^0$	-1.03
H_i^+	-3.60	$(2\text{Mg}_{\text{Ga}2} + V_{\text{O}3})^0$	-1.06

The calculated defect formation energies along with the binding energies of defect pairs are used as an input into our thermodynamic modeling^{51,52}, which yields quantitative defect concentrations, doping limits, and the position of the Fermi level E_F as function of dopant (Mg) concentration, the partial pressures of oxygen ($p\text{O}_2$), hydrogen ($p\text{H}_2$) or water vapor ($p\text{H}_2\text{O}$), and the temperature (T). The Fermi level is obtained as a self-consistent solution that observes the charge balance between defect charges and free carriers, while the defect concentrations are obtained from the defect formation energies for the same E_F . The chemical potentials $\mu_i = \mu_i^0 + \Delta\mu_i$ are expressed by the deviation $\Delta\mu_i$ from to the elemental reference energy μ_i^0 . Using the FERE values of Ref.⁵⁰, we obtain the formation enthalpy of Ga_2O_3 as $\Delta H_f(\text{Ga}_2\text{O}_3) = 2\Delta\mu_{\text{Ga}} + 3\Delta\mu_{\text{O}} = -11.26$ eV, which defines the relationship between Ga and O chemical potentials under the phase-coexistence of Ga_2O_3 . Similarly, using the tabulated⁵³ formation enthalpy of water vapor, we have $\Delta H_f(\text{H}_2\text{O}) = -2.48$ eV = $2\Delta\mu_{\text{H}} + \Delta\mu_{\text{O}} - \Delta\mu_{\text{H}_2\text{O}}$, where the $\Delta\mu$ values for the gas phases are calculated as function of T and partial pressure via the ideal gas equations with the tabulated standard enthalpies and entropies for 298K and 1 atm (note, $\Delta\mu_{\text{O}} = \frac{1}{2} \Delta\mu_{\text{O}_2}$ and $\Delta\mu_{\text{H}} = \frac{1}{2} \Delta\mu_{\text{H}_2}$). Similar thermodynamic simulations have been successfully employed in the past in other oxides to quantitatively predict carrier concentrations as a function of synthesis and measurement conditions, for example in case of the non-equilibrium origin of conductivity in Ga doped ZnO ⁵⁴.

Growth step: In Ga_2O_3 , as in other wide gap oxides, it is generally observed that annealing in oxygen rich environment reduces the free electron density, while annealing in hydrogen rich environment increases it¹. This behavior reflects general doping principles⁵⁵, where O-rich conditions reduce the formation energy of electron compensating defects like cation vacancies and O interstitials. H-rich environments promote the formation of donor-like H interstitials⁵⁶ but at the same time, exposure to H_2 gas also creates O-poor reducing conditions due to the gas phase equilibrium with water vapor, a well-established process that is frequently used in solid state chemistry⁵⁷. These reducing conditions generally favor n -type conductivity. According to the doping principles, the increased Fermi energy in n -type material reduces the formation energy of acceptor-type dopants, thereby enhancing their solubility. Finally, the mobile nature of H interstitials allows to exploit non-equilibrium processing, such as the removal of hydrogen by annealing while the equilibration of other processes remains suppressed, like the exsolution of acceptor dopants or the formation of compensating intrinsic defects⁴⁴. These concepts are exploited in our initial growth step illustrated in Fig. 2.

Figure 2a shows the equilibrium solubility of Mg as function of temperature and $p\text{O}_2$. Under equilibrium conditions, Hydrogen addition is equivalent to maintaining a certain partial pressure $p\text{H}_2\text{O}$ of water vapor, and the hydrogen chemical potential ($\Delta\mu_{\text{H}}$) is determined by the gas phase equilibrium as described above. In Fig. 2a, we used $p\text{H}_2\text{O} = 10^{-5}$ atm as an estimated upper bound for a typical physical vapor deposition (PVD) process such as molecular beam epitaxy (MBE), but the solubility of Mg is barely affected at this low level of hydrogen addition. The Mg equilibrium solubility increases with increasing temperature and decreasing $p\text{O}_2$ (both of which

reduce $\Delta\mu_{\text{O}}$) as expected from the doping principles and remains in the sub-percent range except under extreme reducing conditions.

Figure 2b shows defect equilibria as function of the Mg doping level and the hydrogen chemical potential $\Delta\mu_{\text{H}}$, which is controlled by $p_{\text{H}_2\text{O}}$ (*cf.* left and right vertical axes in Fig 2b), assuming growth conditions at $T_{\text{g}} = 600$ °C and $p_{\text{O}_2} = 10^{-9}$ atm, as representative for low T and moderate p_{O_2} conditions for PVD (MBE) growth of Ga_2O_3 ⁵⁸. The solid black line in Fig. 2b marks the equilibrium thermodynamic solubility limit of Mg in Ga_2O_3 determined by the competing phase MgGa_2O_4 . Within the range of data shown in Fig 2b, the Mg chemical potential does not exceed the bounds determined by $\text{Mg}(\text{OH})_2$, MgH_2 , MgO , and metallic Mg. We observe that significant increases of the Mg solubility occur at $p_{\text{H}_2\text{O}} > 10^{-5}$ atm, reaching about $\text{Mg}/(\text{Mg}+\text{Ga}) = 0.1\%$ at $p_{\text{H}_2\text{O}} = 1$ atm, which is feasible in atmospheric pressure chemical vapor deposition processes (APCVD) of $\beta\text{-Ga}_2\text{O}_3$ ^{59,60}. Even higher Mg solubilities could result from using an activated source, where the H chemical potential $\Delta\mu_{\text{H}}$ can exceed the thermodynamic limits. Such hydrogen plasma has been successfully used in the past during atomic layer deposition (ALD) growth of AlN ⁶¹ and for SiC surface cleaning prior to molecular beam epitaxy (MBE) growth of GaN ⁶². In Figure 2b and the following discussion we consider non-equilibrium Mg concentrations up to 10%, since in thin-film growth the thermodynamic solubility limit can often be exceeded due to slow exsolution kinetics⁶³. For experimental reference, we note that in an ion implantation study²⁶ Mg dopant concentration up to $1.5 \times 10^{19} \text{ cm}^{-3}$ (about 0.05% of the $3.82 \times 10^{22} \text{ cm}^{-3}$ Ga sites) has been achieved in bulk substrates, and it is expected that still much higher concentrations are achievable in thin film growth.

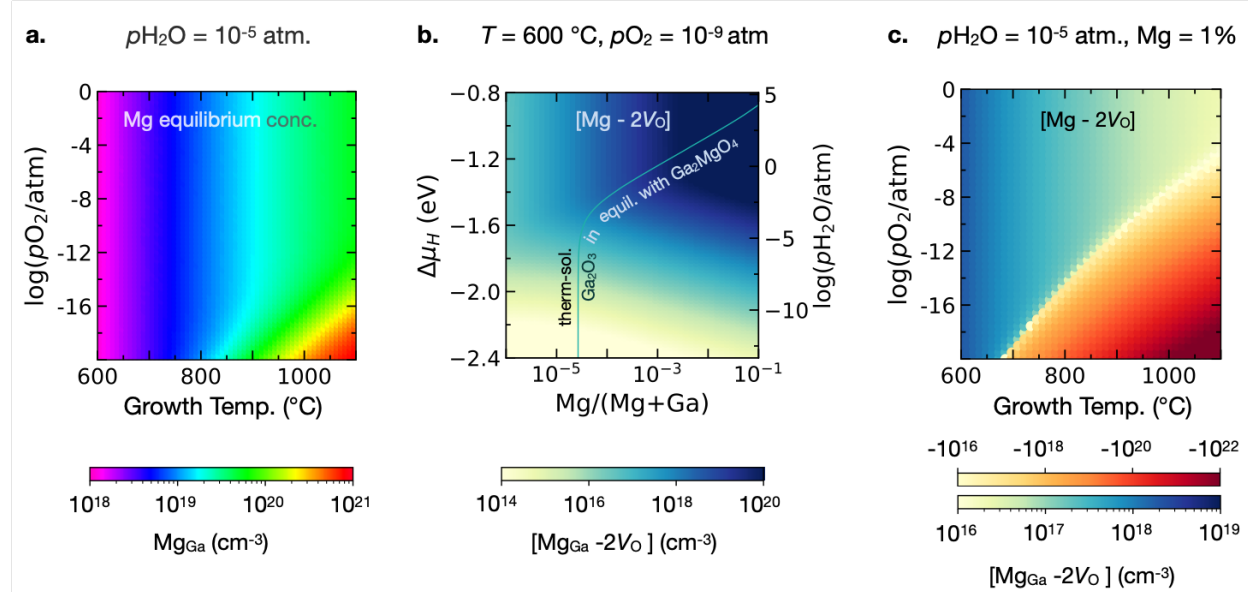


Figure 2. Growth step: (a) Predicted Mg_{Ga} defect concentration as function of growth temperature (T_{g}) and O_2 partial pressure (p_{O_2}). (b) Defect equilibria as a function of the $\text{Mg}/(\text{Mg}+\text{Ga})$ ratio and the water vapor partial pressure ($p_{\text{H}_2\text{O}}$) under O-poor growth conditions typical for thin film growth. The solid line shows the Mg solubility limit and the color scale shows the dopant-defect difference concentration $[\text{Mg}_{\text{Ga}} - 2V_{\text{O}}]$. (c) $[\text{Mg}_{\text{Ga}} - 2V_{\text{O}}]$ as function of T_{g} and p_{O_2} at 1% Mg doping.

Besides Mg solubility considerations, growth under hydrogen addition could also be utilized to minimize the contribution of intrinsic defects to the acceptor compensation⁴³. If the compensation is dominated by H_i donors, the Mg acceptors could be activated by annealing out the hydrogen, proposed that the intrinsic defects would not re-equilibrate (see discussion below). To quantify this effect, we define the dopant-defect difference concentration $[Mg_{Ga} - 2V_O]$ with the results shown as a color scale in Figure 2b. The significance of this number is that it equals the hypothetical net acceptor concentration if all hydrogen could be purged during the high temperature annealing step without introducing additional V_O defects. Therefore, we will refer to it as the “precursor” acceptor concentration. The color scale in Fig 2b shows $[Mg_{Ga} - 2V_O]$ increasing moderately with Mg composition and rather strongly with p_{H_2O} , and the associated H chemical potential. Thus, the hydrogen serves to reduce the intrinsic compensation mechanism, thereby maximizing the precursor acceptor concentration for the subsequent annealing step. Figure 2c explores the dependence of the $[Mg_{Ga} - 2V_O]$ concentration as function of T and p_{O_2} at fixed p_{H_2O} and Mg composition. We observe that this precursor acceptor density decreases with increasing growth temperature. Also, for too reducing conditions (too high T_g or too low p_{O_2}), $[Mg_{Ga} - 2V_O]$ becomes negative, implying that the system would remain n -type even if all H were removed. Thus, low temperature conditions are favorable for the initial growth step.

Annealing step: In the post-growth annealing step (Fig. 3), H-poor/O-rich conditions are considered, analogous to the H-poor/N-rich conditions used for Mg acceptor activation in GaN^{40,41}. At 600°C, the O chemical potential increases from $\Delta\mu_O = -1.72$ to -0.94 eV as p_{O_2} increases from 10^{-9} atm in the growth step to 1 atm considered here for the O-rich annealing condition. Apart from increasing the formation energy of compensating O vacancies, the result is also a reduction of the H chemical potential from $\Delta\mu_H = -1.68$ (growth step with $p_{O_2} = 10^{-9}$ atm and $p_{H_2O} = 10^{-5}$ atm) to -2.33 eV when taking $p_{H_2O} = 10^{-8}$ atm (10 ppb) for purified O_2 at 1 atm used in the annealing step. Additionally, increasing the temperature during annealing lowers both $\Delta\mu_O$ and $\Delta\mu_H$, e.g., by about 0.4 eV between 600 and 900°C. Thus, the Mg acceptor activation relies on both suppressing compensation by V_O and reduction of the H concentration during annealing. Kinetically, the annealing conditions must also be such that H is sufficiently mobile to diffuse out while Mg remains immobile so to prevent Mg segregation. The rationale for choosing the present process parameters comes from recent Mg doping studies^{26,28,64}, indicating that Mg needs $T > 800$ °C to become mobile, and calculations of a small migration barrier of 0.34 eV²² for H_i^+ indicating sufficiently fast H diffusion. A more subtle question is whether the annealing process can be performed such that the O vacancy concentrations from the growth step are maintained or whether they equilibrate. Since it could be feasible to realize either situation, we will consider both scenarios.

Equilibrium annealing with V_O equilibration. In this scenario, only the total Mg concentration is carried over from the growth step, and all other degrees of freedom are equilibrated, while switching to the O-rich/H-poor regime ($p_{O_2} = 1$ atm, $p_{H_2O} = 10^{-8}$ atm). Thus, in this scenario, the H addition of the growth step is relevant only in so far it supports the incorporation of Mg in the Ga_2O_3 lattice. Figure 3a shows the resulting net acceptor concentration $[Mg - 2V_O - H_i]$ obtained from thermodynamic modeling as function of annealing temperature. As the annealing temperature increases, H is purged out of the system, resulting in an increasing concentration of uncompensated net Mg acceptors, making the system net p -type in the sense of a positive value

of the $[Mg - 2V_o - H_i]$ concentration difference. However, as the annealing temperature is increased, the O vacancy concentration also increases (driven by a reduction of $\Delta\mu_o$) and therefore, there is a tipping point with respect to the annealing temperature above which O vacancies compensate the Mg acceptors and make the system net n -type.

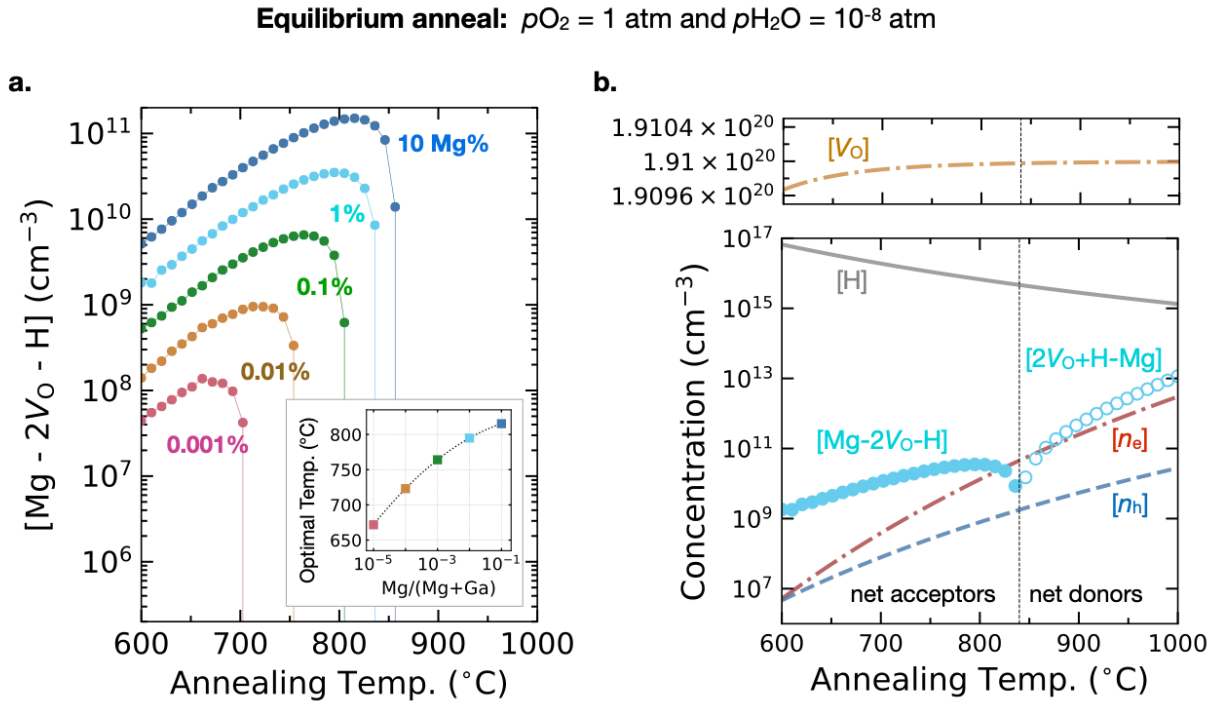


Figure 3. *Equilibrium annealing step with V_o equilibration*: (a) Predicted net acceptor concentration $[Mg - 2V_o - H_i]$ for the O-rich/H-poor annealing step. The inset shows the dependence of the optimal annealing temperature T_a on the Mg concentration. (b) The detailed defect equilibrium for $Mg/(Mg+Ga) = 1\%$. The vertical dotted line indicates the crossover from net p -type to net n -type.

While the Fermi energy remains in the mid-gap region during annealing, it exhibits a small shift towards higher energies with increasing temperature, enough to affect the ratio between charged and ionized defects (Mg_{Ga}^0 vs Mg_{Ga}^- and V_o^0 vs V_o^{2+}). These changes in the order of 10^{10} cm^{-3} contribute to the charge balance and, ultimately, cause the crossover from net p -type to net n -type. As seen in the inset of Fig 3a, the optimum annealing temperature, i.e., the temperature at which the net p -type doping is maximized, increases from 670 to 820 °C with increasing Mg composition from 0.001% to 10%. The resulting net acceptor concentrations in the range of $10^8 - 10^{11} \text{ cm}^{-3}$ are rather low, but the type conversion to net p -type is a significant hallmark, since it affords very low free electron densities at device operating conditions (see below). The resulting net acceptor density $[Mg - 2V_o - H_i]$ is much lower than the precursor acceptor density $[Mg - 2V_o]$ determined above for the growth step. This incomplete acceptor activation is due to the fact that not all hydrogen is purged, but also due to an increase of the concentration of compensating O vacancies during the annealing step, resulting from a lowered formation energy of V_o^{2+} as E_F is reduced, even as $\Delta\mu_o$ is increased compared to the growth step.

(Hence, a higher net p -type doping is expected for the case when V_O equilibration is suppressed, as discussed below.) The residual H concentration ranges from 4.3×10^{16} to $4.5 \times 10^{17} \text{ cm}^{-3}$ at the optimal temperature for the Mg doping level between 0.001% and 10%, respectively.

Non-equilibrium annealing without V_O equilibration. We are also considering possible non-equilibrium annealing conditions in Ga_2O_3 , even though these might be more difficult to realize experimentally. Under the assumption that O diffusion is much slower than that of H, the annealing process could be performed such that H diffuses out while the O vacancy formation does not have enough time to re-equilibrate. In this scenario, the V_O concentration is fixed to that of the preceding growth step, and the H addition during growth has higher significance than in the equilibrium annealing case, since it serves to reduce the compensation by V_O and thereby increase the precursor acceptor density $[\text{Mg} - 2V_O]$ (cf. Fig. 2b). The calculated values of O vacancy migration barriers in the literature⁶⁵ indeed indicate a much lower mobility compared to interstitial hydrogen²². Therefore, non-equilibrium annealing could be feasible if the annealing process is performed sufficiently fast. Even though the total V_O concentration remains constant, the dopant-defect pair association-dissociation process is equilibrated in the simulation, because this process does not require long-range diffusion and should be comparatively fast.

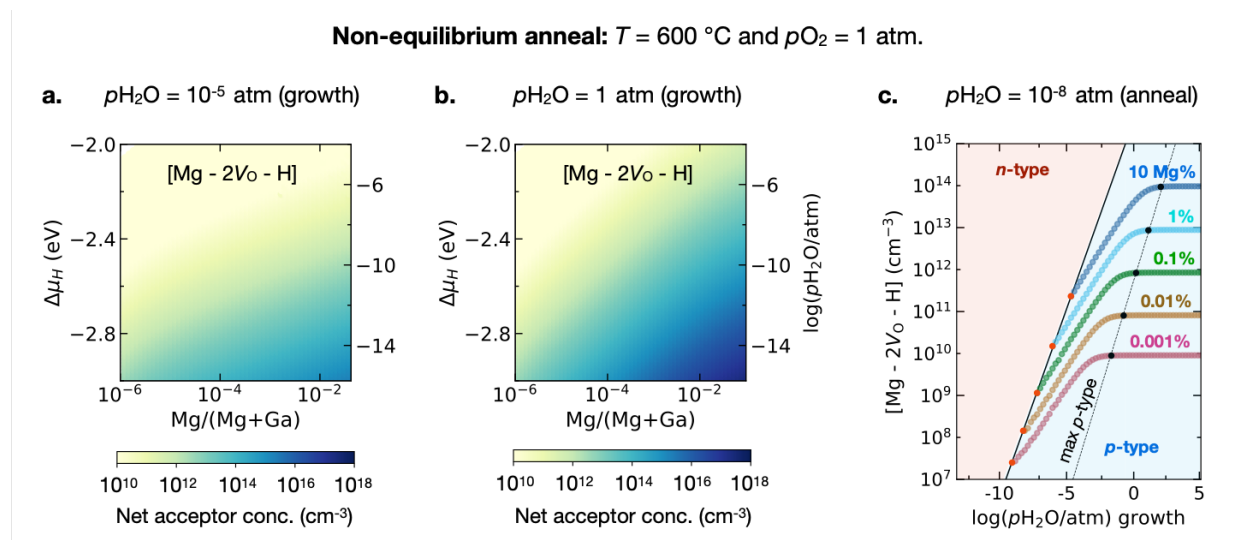


Figure 4. *Non-equilibrium annealing step without V_O equilibration:* Predicted net acceptor concentration $[\text{Mg} - 2V_O - H_i]$ under O-rich/H-poor annealing conditions at $T_a = 600 \text{ }^\circ\text{C}$ and $p\text{O}_2 = 1 \text{ atm}$, as function of Mg-doping level and $p\text{H}_2\text{O}$ (controlling $\Delta\mu_H$) during the anneal. Non-equilibrium conditions are assumed such that the O-vacancy concentration of the preceding growth step is maintained. The underlying growth step conditions are consistent with Fig. 2b, i.e., $T_g = 600 \text{ }^\circ\text{C}$, $p\text{O}_2 = 10^{-9} \text{ atm}$, with hydrogen exposure during growth taken as $p\text{H}_2\text{O} = 10^{-5} \text{ atm}$ for Fig. 4a and 1 atm for Fig. 4b. The dependence of the net acceptor concentration on $p\text{H}_2\text{O}$ during the growth step is shown in (c).

Figure 4 shows the predicted net acceptor concentration $[\text{Mg} - 2V_O - H_i]$ for annealing without V_O equilibration. The underlying growth step conditions are identical to those considered above (cf. Fig. 2b), i.e., $T_g = 600 \text{ }^\circ\text{C}$, $p\text{O}_2 = 10^{-9} \text{ atm}$, with hydrogen exposure during growth taken as $p\text{H}_2\text{O} = 10^{-5} \text{ atm}$ for Fig. 4a and 1 atm for Fig. 4b. For the annealing conditions, we maintain the same temperature, $T_a = 600 \text{ }^\circ\text{C}$ and use O-rich conditions with $p\text{O}_2 = 1 \text{ atm}$ as in the equilibrium

annealing case above. According to migration barrier calculations,⁶⁵ O vacancies are beginning to become mobile at this temperature. Note that the model here assumes equilibration of O vacancies during growth but not during annealing, despite the fact that both processes occur at same temperature. This assumption can be justified by the general observations that the surface kinetics during growth is usually faster than in the bulk, and the diffusion distance required for equilibration is much larger for the completed film during annealing than it is during deposition^{66,67}.

We observe in Fig. 4 the expected increase of the net acceptor density with increasing Mg-doping level and decreasing H-chemical potential $\Delta\mu_H$, which is determined by the corresponding p_{H_2O} during the annealing. Compared to the annealing with V_O equilibration, the net acceptor density increases considerably under otherwise identical conditions. For example, for growth with 1% Mg doping and $p_{H_2O} = 10^{-5}$ atm, we obtain $[Mg - 2V_O - H_i] \approx 10^{11}$ cm⁻³ (Fig 4a) after non-equilibrium annealing at 600 °C and $p_{H_2O} = 10^{-8}$ atm (purified O₂), about 1-2 orders of magnitude higher than in case of annealing with V_O equilibration (*cf.* Fig. 3a). Higher net acceptor densities, up to 10^{14} cm⁻³ (Fig 4b), result when the preceding growth step is performed under very H rich conditions with $p_{H_2O} = 1$ atm. These results suggest that H addition during growth is most impactful when choosing deposition techniques that allow for high H₂O partial pressures. As seen in Fig 4c, a minimum p_{H_2O} must be supplied during growth to enable *p*-type conversion during non-equilibrium annealing, for example $p_{H_2O} = 10^{-7}$ atm for 1% Mg doping. In the absence of H₂O addition, the compensation is dominated by O vacancies during growth, preventing type conversion during annealing. The H₂O partial pressure required to achieve maximal net *p*-type doping increases from 10^{-2} atm to 10^2 atm with increasing Mg concentration from 0.001% to 10%. These results provide theoretical guidance for optimization of the post-growth annealing step of Mg-doped Ga₂O₃.

Quenching step: Finally, we are considering the doping situation under device operating conditions. It is assumed that the defect concentrations from the preceding annealing step are quenched-in, and no equilibration with the environment takes place (e.g., H uptake from ambient precluded by encapsulation). During this step, only the electronic degrees of freedom equilibrate, i.e., the Fermi level E_F and the corresponding electron (n_e) and hole (n_h) concentrations. We are considering elevated device operating temperatures T_o , as relevant for Ga₂O₃ high-power and high-temperature electronics applications⁶⁸. Figure 5a shows the Fermi level as function of T_o and the Mg doping level for the case of V_O equilibration during the preceding annealing step at the optimum temperature T_a for any given Mg doping level (*cf.* Fig. 3 insert). Figures 5b and 5c are for the case of non-equilibrium annealing at 600 °C, where the growth step was performed at the same temperature with $p_{H_2O} = 10^{-5}$ atm and 1 atm, respectively (*cf.* Fig. 4a and 4b). In all cases, the annealing conditions before the quench were taken at $p_{O_2} = 1$ atm and $p_{H_2O} = 10^{-8}$ atm as discussed above.

In Fig. 5a, we observe a moderate reduction of E_F with the Mg doping level. The Fermi level increases with operating temperature T_o , but remains within the lower half of the band gap (net *p*-type). While the absolute hole carrier concentration remains very low (below 10^6 cm⁻³), the more important finding is here that the electron concentration remains negligible (below 10^3 cm⁻³) up to 400 °C. The suppression of the electron density is an important feature of the type conversion, and our simulations suggest that the proposed growth-annealing process is suitable to effectively suppress the electron conductivity, e.g., for the purpose to minimize the associated leakage

currents in device applications. However, achieving actual p -type conductivity is a much greater challenge. The quenching from the non-equilibrium annealing step, shown in Figs. 5b and 5c, affords a stronger Fermi level reduction than the annealing with V_O equilibration. Even then, however, the corresponding hole concentrations are only about 10^8 cm^{-3} at $T_o = 400 \text{ }^\circ\text{C}$ (Fig. 5c). Since holes tend to form localized polarons rather than acting as band-like free carriers, the p -type conductivity is further limited by the hole mobility. Based on a predicted polaron hopping barrier of 0.4 eV, the mobility was estimated in Ref.⁶⁹ as $10^{-6} \text{ cm}^2 \text{ V}^{-1} \text{ s}^{-1}$ at room temperature, which could increase to about $10^{-3} \text{ cm}^2 \text{ V}^{-1} \text{ s}^{-1}$ at $400 \text{ }^\circ\text{C}$, resulting in a conductivity $\sigma \approx 10^{-14} \text{ S/cm}$ for the above mentioned hole density. These rough estimates illustrate the challenges for achieving significant p -type conductivity even at elevated temperatures and under optimistic assumptions about suppressing the V_O compensation mechanism.

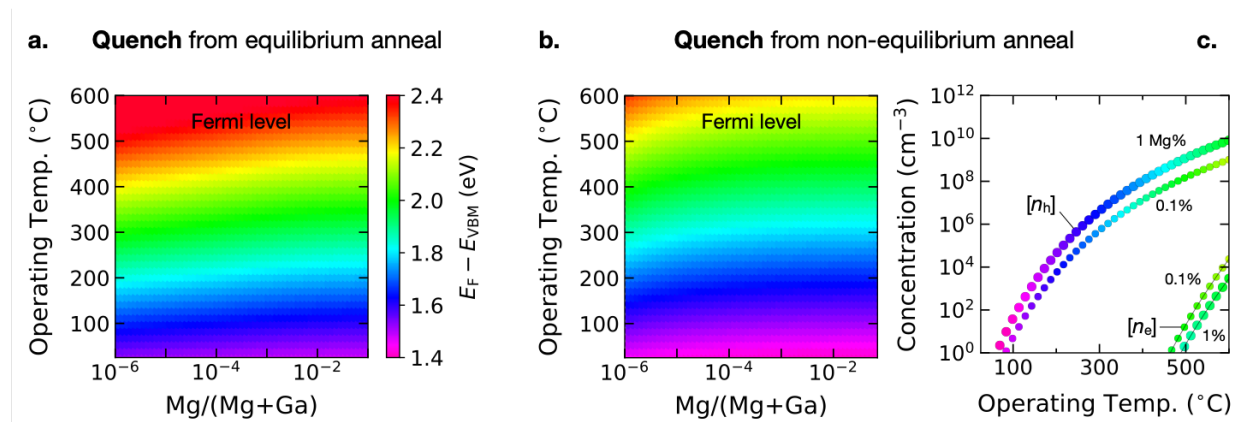


Figure 5. *Quench step*: (a) Predicted Fermi level ($E_F - E_{VBM}$) as function of operating temperature T_o and Mg doping level, after quenching-in the defect concentrations from the preceding annealing step with V_O equilibration at the optimal T_a for each Mg concentration (inset in Fig. 3a). (b) Fermi level after quench from the preceding non-equilibrium annealing step at $T = 600^\circ\text{C}$ with growth at $p\text{H}_2\text{O} = 10^{-5} \text{ atm}$ (cf. Fig. 4a), and (c) with growth at $p\text{H}_2\text{O} = 1 \text{ atm}$ (cf. Fig. 4b). In (c), the T_o dependence of the electron $[n_e]$ and hole $[n_h]$ concentrations corresponding to the respective E_F is shown for Mg concentrations of 0.1% and 1%.

Conclusions: We performed a thermodynamic simulation of a synthesis process (growth-annealing-quench sequence) for hydrogen-assisted magnesium acceptor doping in Ga_2O_3 based on defect energies obtained from first principles calculations. During the growth step, the thermodynamic solubility limit of Mg acceptor dopants is significantly increased for partial pressures above $p\text{H}_2\text{O} > 10^{-5} \text{ atm}$. The H exposure during growth also serves to reduce the acceptor compensation through V_O defects. The annealing step at O-rich/H-poor conditions ($p\text{O}_2 = 1 \text{ atm}$ and $p\text{H}_2\text{O} = 10^{-8} \text{ atm}$) can produce a doping type conversion from net n - to net p -type, and we consider both cases with and without V_O re-equilibration. For the case with V_O equilibration, there is an optimal annealing temperature at which the net p -type doping is maximized, e.g., about $800 \text{ }^\circ\text{C}$ for 1% Mg doping, but too high annealing temperatures result in reversion to net n -type. The net p -type doping can be further increased if the V_O equilibration can be suppressed, e.g., in rapid thermal processing at lower temperature ($600 \text{ }^\circ\text{C}$). In this case, the H addition during growth not only supports the Mg solubility, but is also essential to suppress the

intrinsic O vacancy compensation mechanism. Even though neither scenario creates significant p -type conductivity, the doping type conversion and associated drop of the Fermi level present important opportunities for device design, allowing to create a significant built-in field in a p - n junction with an adjoining n -type material, and greatly suppressing the free electron density. The specific predictions of suitable synthesis process conditions presented in this paper could guide the fabrication of current blocking layers, for example in normally-off (enhancement-mode) vertical Ga₂O₃ based MOSFET and as a guard ring for edge termination in such transistors, and in Schottky barrier diodes with increased breakdown voltage.

Computational details: The first-principles calculations were performed using the projector augmented wave (PAW) method⁷⁰ as implemented in the VASP (Vienna Ab-initio Simulation Package) code⁷¹ for DFT⁷², hybrid-DFT⁷³, and GW⁷⁴ calculations. The generalized gradient approximation (GGA) of Ref⁷⁵ was used for DFT exchange and correlation and the HSE06^{76,77} functional for hybrid functional calculations. The defect formation energies and charge transition levels (in both DFT and hybrid-DFT) are calculated in 160 atom defect supercells with a Γ centered 2×2×2 k-mesh, using our recently developed automated defect framework⁷⁸. The PAW potentials “Ga_d”, “O”, “O_s”, “Mg_pv”, and “H” of the VASP 4.6 distribution were used. For structures without hydrogen, the soft “O_s” potential was employed with a plane wave energy cutoff of 340 eV. Previous tests have confirmed that such calculations are accurate for sufficiently large interatomic distances.⁴⁹ Due to the presence of short O-H bonds for which the soft potential may not be accurate, we used the standard “O” potential with 520 eV cutoff for structures with hydrogen. Finite size corrections are applied as described in Ref.⁷⁹ In the hybrid-DFT calculations, the HSE06 functional^{76,77} is employed with $\alpha = 0.3$ and $\mu = 0.2 \text{ \AA}^{-1}$ for the fractional Fock exchange and the range separation parameters, respectively. For the DFT bandgap correction, GW calculations⁸⁰ gives the individual band edge shifts of $\Delta E_{\text{VBM}} = -1.82 \text{ eV}$ and $\Delta E_{\text{CBM}} = +1.1 \text{ eV}$ relative to DFT-GGA, resulting in the bandgap value of 4.96 eV. The FERRE reference elemental chemical potentials of Ref⁵⁰ are used for Ga, O, and Mg. For hydrogen, we determined here the value $\mu_{\text{H}}^0 = -3.49 \text{ eV}$ by fitting against the tabulated formation enthalpies⁵³ of the following compounds, H₂O (ice I_h), LiH, MgH₂, LiOH and Mg(OH)₂. The temperature dependence of the CBM was taken from Ref²³, where it was determined from molecular dynamics simulations.

Acknowledgements: This work was funded by the U.S. Department of Energy (DOE), through the Laboratory Directed Research and Development Program of the National Renewable Energy Laboratory (NREL), and by the DOE Advanced Manufacturing Office of the Office of Energy Efficiency and Renewable Energy (EERE). The Alliance for Sustainable Energy, LLC, operates and manages NREL under contract DE-AC36-08GO28308. This work used High-Performance Computing resources at NREL, sponsored by DOE-EERE. The views expressed in the article do not necessarily represent the views of the DOE or the U.S. government.

References:

1. Pearton, S. J. *et al.* A review of Ga₂O₃ materials, processing, and devices. *Appl. Phys. Rev.* **5**, 011301 (2018).
2. Reese, S. B., Remo, T., Green, J. & Zakutayev, A. How Much Will Gallium Oxide Power Electronics Cost? *Joule* **3**, 903–907 (2019).
3. Baldini, M., Galazka, Z. & Wagner, G. Recent progress in the growth of β -Ga₂O₃ for power electronics applications. *Mater. Sci. Semicond. Process.* **78**, 132–146 (2018).
4. Liu, Z. *et al.* Review of gallium oxide based field-effect transistors and Schottky barrier diodes. *Chinese Phys. B* **28**, 017105 (2019).
5. Chabak, K. D. *et al.* Lateral β -Ga₂O₃ field effect transistors. *Semicond. Sci. Technol.* **35**, 013002 (2020).
6. Xu, J., Zheng, W. & Huang, F. Gallium oxide solar-blind ultraviolet photodetectors: a review. *J. Mater. Chem. C* **7**, 8753–8770 (2019).
7. Chen, X., Ren, F., Gu, S. & Ye, J. Review of gallium-oxide-based solar-blind ultraviolet photodetectors. *Photonics Res.* **7**, 381 (2019).
8. Chen, X., Ren, F., Ye, J. & Gu, S. Gallium oxide-based solar-blind ultraviolet photodetectors. *Semicond. Sci. Technol.* **35**, 023001 (2020).
9. Hofer, U., Frank, J. & Fleischer, M. High temperature Ga₂O₃-gas sensors and SnO₂-gas sensors: a comparison. *Sensors Actuators B Chem.* **78**, 6–11 (2001).
10. Afzal, A. β -Ga₂O₃ nanowires and thin films for metal oxide semiconductor gas sensors: Sensing mechanisms and performance enhancement strategies. *J. Mater.* **5**, 542–557 (2019).
11. Minami, T., Nishi, Y. & Miyata, T. High-Efficiency Cu₂O-Based Heterojunction Solar Cells Fabricated Using a Ga₂O₃ Thin Film as N-Type Layer. *Appl. Phys. Express* **6**, 044101 (2013).
12. Chua, D., Kim, S. B. & Gordon, R. Enhancement of the open circuit voltage of Cu₂O/Ga₂O₃ heterojunction solar cells through the mitigation of interfacial recombination. *AIP Adv.* **9**, 055203 (2019).
13. Li, Y. *et al.* Efficient Assembly of Bridged β -Ga₂O₃ Nanowires for Solar-Blind Photodetection. *Adv. Funct. Mater.* **20**, 3972–3978 (2010).
14. Yang, J.-B. *et al.* Resistive switching characteristics of gallium oxide for nonvolatile memory application. *Thin Solid Films* **529**, 200–204 (2013).
15. Higashiwaki, M. *et al.* Recent progress in Ga₂O₃ power devices. *Semicond. Sci. Technol.* **31**, 034001 (2016).
16. Pearton, S. J., Ren, F., Tadjer, M. & Kim, J. Perspective: Ga₂O₃ for ultra-high power rectifiers and MOSFETS. *J. Appl. Phys.* **124**, 220901 (2018).
17. Wong, M. H., Goto, K., Murakami, H., Kumagai, Y. & Higashiwaki, M. Current Aperture Vertical β -Ga₂O₃ MOSFETs Fabricated by N- and Si-Ion Implantation Doping. *IEEE Electron Device Lett.* **40**, 431–434 (2019).
18. Hu, Z. *et al.* Enhancement-Mode Ga₂O₃ Vertical Transistors With Breakdown Voltage >1 kV. *IEEE Electron Device Lett.* **39**, 869–872 (2018).
19. Ueda, N., Hosono, H., Waseda, R. & Kawazoe, H. Synthesis and control of conductivity of ultraviolet transmitting β -Ga₂O₃ single crystals. *Appl. Phys. Lett.* **70**, 3561–3563 (1997).
20. Sasaki, K. *et al.* Device-Quality β -Ga₂O₃ Epitaxial Films Fabricated by Ozone Molecular Beam Epitaxy. *Appl. Phys. Express* **5**, 035502 (2012).
21. Ahmadi, E. *et al.* Ge doping of β -Ga₂O₃ films grown by plasma-assisted molecular beam epitaxy. *Appl. Phys. Express* **10**, 041102 (2017).
22. Varley, J. B., Weber, J. R., Janotti, A. & Van de Walle, C. G. Oxygen vacancies and

- donor impurities in β -Ga₂O₃. *Appl. Phys. Lett.* **97**, 142106 (2010).
23. Lany, S. Defect phase diagram for doping of Ga₂O₃. *APL Mater.* **6**, 046103 (2018).
 24. Varley, J. B., Peelaers, H., Janotti, A. & Van de Walle, C. G. Hydrogenated cation vacancies in semiconducting oxides. *J. Phys. Condens. Matter* **23**, 334212 (2011).
 25. Kyrtsov, A., Matsubara, M. & Bellotti, E. On the feasibility of p-type Ga₂O₃. *Appl. Phys. Lett.* **112**, 032108 (2018).
 26. Wong, M. H. *et al.* Acceptor doping of β -Ga₂O₃ by Mg and N ion implantations. *Appl. Phys. Lett.* **113**, 102103 (2018).
 27. Lyons, J. L. A survey of acceptor dopants for β -Ga₂O₃. *Semicond. Sci. Technol.* **33**, 05LT02 (2018).
 28. Peelaers, H., Lyons, J. L., Varley, J. B. & Van de Walle, C. G. Deep acceptors and their diffusion in Ga₂O₃. *APL Mater.* **7**, 022519 (2019).
 29. Chikoidze, E. *et al.* Enhancing the intrinsic p-type conductivity of the ultra-wide bandgap Ga₂O₃ semiconductor. *J. Mater. Chem. C* **7**, 10231–10239 (2019).
 30. Zhang, J., Shi, J., Qi, D.-C., Chen, L. & Zhang, K. H. L. Recent progress on the electronic structure, defect, and doping properties of Ga₂O₃. *APL Mater.* **8**, 020906 (2020).
 31. McCluskey, M. D. Point defects in Ga₂O₃. *J. Appl. Phys.* **127**, 101101 (2020).
 32. Feng, Z., Bhuiyan, A. F. M. A. U., Kalarickal, N. K., Rajan, S. & Zhao, H. Mg acceptor doping in MOCVD (010) β -Ga₂O₃. *Appl. Phys. Lett.* **117**, 222106 (2020).
 33. Lenyk, C. A., Gustafson, T. D., Basun, S. A., Halliburton, L. E. & Giles, N. C. Experimental determination of the (0/-) level for Mg acceptors in β -Ga₂O₃ crystals. *Appl. Phys. Lett.* **116**, 142101 (2020).
 34. Su, Y. *et al.* Deep level acceptors of Zn-Mg divalent ions dopants in β -Ga₂O₃ for the difficulty to p-type conductivity. *J. Alloys Compd.* **782**, 299–303 (2019).
 35. Ho, Q. D., Frauenheim, T. & Deák, P. Theoretical confirmation of the polaron model for the Mg acceptor in β -Ga₂O₃. *J. Appl. Phys.* **124**, 145702 (2018).
 36. Gake, T., Kumagai, Y. & Oba, F. First-principles study of self-trapped holes and acceptor impurities in Ga₂O₃ polymorphs. *Phys. Rev. Mater.* **3**, 44603 (2019).
 37. Skachkov, D. & Lambrecht, W. R. L. Computational study of electron paramagnetic resonance parameters for Mg and Zn impurities in β -Ga₂O₃. *Appl. Phys. Lett.* **114**, 202102 (2019).
 38. Frodason, Y. K., Johansen, K. M., Vines, L. & Varley, J. B. Self-trapped hole and impurity-related broad luminescence in β -Ga₂O₃. *J. Appl. Phys.* **127**, 075701 (2020).
 39. Kotecha, R., Metzger, W., Mather, B., Narumanchi, S. & Zakutayev, A. Modeling and Analysis of Gallium Oxide Vertical Transistors. *ECS J. Solid State Sci. Technol.* **8**, Q3202–Q3205 (2019).
 40. Nakamura, S., Iwasa, N., Senoh, M. & Mukai, T. Hole Compensation Mechanism of P-Type GaN Films. *Jpn. J. Appl. Phys.* **31**, 1258–1266 (1992).
 41. Nakamura, S., Mukai, T., Senoh, M. & Iwasa, N. Thermal Annealing Effects on P-Type Mg-Doped GaN Films. *Jpn. J. Appl. Phys.* **31**, L139–L142 (1992).
 42. Vechten, J. A. Van, Zook, J. D., Horning, R. D. & Goldenberg, B. Defeating Compensation in Wide Gap Semiconductors by Growing in H that is Removed by Low Temperature De-Ionizing Radiation. *Jpn. J. Appl. Phys.* **31**, 3662–3663 (1992).
 43. Neugebauer, J. & Van De Walle, C. G. Role of hydrogen in doping of GaN. *Appl. Phys. Lett.* **68**, 1829–1831 (1996).
 44. Neumark, G. F. Wide bandgap light-emitting devices materials and doping problems. *Mater. Lett.* **30**, 131–135 (1997).
 45. Fioretti, A. N. *et al.* Effects of Hydrogen on Acceptor Activation in Ternary Nitride Semiconductors. *Adv. Electron. Mater.* **3**, 1600544 (2017).
 46. Pan, J. *et al.* Interplay between Composition, Electronic Structure, Disorder, and Doping due to Dual Sublattice Mixing in Nonequilibrium Synthesis of ZnSnN₂:O. *Adv. Mater.* **31**,

- 1807406 (2019).
47. Kim, J. *et al.* Influence of hydrogen and oxygen on the structure and properties of sputtered magnesium zirconium oxynitride thin films. *J. Mater. Chem. A* **8**, 9364–9372 (2020).
 48. Kananen, B. E. *et al.* Electron paramagnetic resonance study of neutral Mg acceptors in β -Ga₂O₃ crystals. *Appl. Phys. Lett.* **111**, 072102 (2017).
 49. Peng, H. *et al.* Convergence of density and hybrid functional defect calculations for compound semiconductors. *Phys. Rev. B* **88**, 115201 (2013).
 50. Stevanović, V., Lany, S., Zhang, X. & Zunger, A. Correcting density functional theory for accurate predictions of compound enthalpies of formation: Fitted elemental-phase reference energies. *Phys. Rev. B* **85**, 115104 (2012).
 51. Biswas, K. & Lany, S. Energetics of quaternary III-V alloys described by incorporation and clustering of impurities. *Phys. Rev. B* **80**, 115206 (2009).
 52. Lany, S. Communication: The electronic entropy of charged defect formation and its impact on thermochemical redox cycles. *J. Chem. Phys.* **148**, 071101 (2018).
 53. Wagman, D. D. *et al.* 'The NBS tables of chemical thermodynamic properties: Selected values for inorganic and c1 and c2 organic substances in SI Units'. *J. Phys. Chem. Ref. Data* **11**, Suppl. 2 (1982).
 54. Zakutayev, A., Perry, N. H., Mason, T. O., Ginley, D. S. & Lany, S. Non-equilibrium origin of high electrical conductivity in gallium zinc oxide thin films. *Appl. Phys. Lett.* **103**, 232106 (2013).
 55. Zunger, A. Practical doping principles. *Appl. Phys. Lett.* **83**, 57–59 (2003).
 56. Van de Walle, C. G. & Neugebauer, J. Universal alignment of hydrogen levels in semiconductors, insulators and solutions. *Nature* **423**, 626–628 (2003).
 57. Ingram, B. J., Gonzalez, G. B., Kammler, D. R., Bertoni, M. I. & Mason, T. O. Chemical and structural factors governing transparent conductivity in oxides. *J. Electroceramics* **13**, 167–175 (2004).
 58. Brooks Tellekamp, M., Heinselman, K. N., Harvey, S., Khan, I. S. & Zakutayev, A. Growth and characterization of homoepitaxial β -Ga₂O₃ layers. *J. Phys. D: Appl. Phys.* **53**, 484002 (2020).
 59. Terasako, T., Ichinotani, H. & Yagi, M. Growth of β -gallium oxide films and nanostructures by atmospheric-pressure CVD using gallium and water as source materials. *Phys. Status Solidi Curr. Top. Solid State Phys.* **12**, 985–988 (2015).
 60. Terasako, T., Kawasaki, Y. & Yagi, M. Growth and morphology control of β -Ga₂O₃ nanostructures by atmospheric-pressure CVD. *Thin Solid Films* **620**, 23–29 (2016).
 61. Tian, L. *et al.* Aluminum nitride thin films deposited by hydrogen plasma enhanced and thermal atomic layer deposition. *Surf. Coatings Technol.* **347**, 181–190 (2018).
 62. Lin, M. E. *et al.* GaN grown on hydrogen plasma cleaned 6H-SiC substrates. *Appl. Phys. Lett.* **62**, 702–704 (1993).
 63. González, G. B., Mason, T. O., Okasinski, J. S., Buslaps, T. & Honkimäki, V. Determination of the Solubility of Tin in Indium Oxide Using In Situ and Ex Situ X-Ray Diffraction. *J. Am. Ceram. Soc.* **95**, 809–815 (2012).
 64. Wong, M. H. *et al.* All-ion-implanted planar-gate current aperture vertical Ga₂O₃ MOSFETs with Mg-doped blocking layer. *Appl. Phys. Express* **11**, 064102 (2018).
 65. Kyrtsov, A., Matsubara, M. & Bellotti, E. Migration mechanisms and diffusion barriers of vacancies in Ga₂O₃. *Phys. Rev. B* **95**, 245202 (2017).
 66. Mazzolini, P. & Bierwagen, O. Towards smooth (010) β -Ga₂O₃ films homoepitaxially grown by plasma assisted molecular beam epitaxy: the impact of substrate offset and metal-to-oxygen flux ratio. *J. Phys. D: Appl. Phys.* **53**, 354003 (2020).
 67. Bin Anooz, S. *et al.* Step flow growth of β -Ga₂O₃ thin films on vicinal (100) β -Ga₂O₃ substrates grown by MOVPE. *Appl. Phys. Lett.* **116**, 2–7 (2020).

68. Paret, P. *et al.* Thermal and Thermomechanical Modeling to Design a Gallium Oxide Power Electronics Package. in *2018 IEEE 6th Workshop on Wide Bandgap Power Devices and Applications (WiPDA)* 287–294 (IEEE, 2018). doi:10.1109/WiPDA.2018.8569139.
69. Varley, J. B., Janotti, A., Franchini, C. & Van de Walle, C. G. Role of self-trapping in luminescence and p-type conductivity of wide-band-gap oxides. *Phys. Rev. B* **85**, 081109 (2012).
70. Blöchl, P. E. Projector augmented-wave method. *Phys. Rev. B* **50**, 17953–17979 (1994).
71. Kresse, G. & Furthmüller, J. Efficiency of ab-initio total energy calculations for metals and semiconductors using a plane-wave basis set. *Comput. Mater. Sci.* **6**, 15–50 (1996).
72. Kresse, G. From ultrasoft pseudopotentials to the projector augmented-wave method. *Phys. Rev. B* **59**, 1758–1775 (1999).
73. Paier, J. *et al.* Screened hybrid density functionals applied to solids. *J. Chem. Phys.* **124**, 154709 (2006).
74. Shishkin, M. & Kresse, G. Implementation and performance of the frequency-dependent GW method within the PAW framework. *Phys. Rev. B* **74**, 035101 (2006).
75. Perdew, J. P., Burke, K. & Ernzerhof, M. Generalized Gradient Approximation Made Simple. *Phys. Rev. Lett.* **77**, 3865–3868 (1996).
76. Heyd, J., Scuseria, G. E. & Ernzerhof, M. Hybrid functionals based on a screened Coulomb potential. *J. Chem. Phys.* **118**, 8207–8215 (2003).
77. Heyd, J., Scuseria, G. E. & Ernzerhof, M. Erratum: “Hybrid functionals based on a screened Coulomb potential” [*J. Chem. Phys.* 118, 8207 (2003)]. *J. Chem. Phys.* **124**, 219906 (2006).
78. Goyal, A., Gorai, P., Peng, H., Lany, S. & Stevanović, V. A computational framework for automation of point defect calculations. *Comput. Mater. Sci.* **130**, 1–9 (2017).
79. Lany, S. & Zunger, A. Accurate prediction of defect properties in density functional supercell calculations. *Model. Simul. Mater. Sci. Eng.* **17**, 084002 (2009).
80. Hedin, L. New Method for Calculating the One-Particle Green’s Function with Application to the Electron-Gas Problem. *Phys. Rev.* **139**, A796–A823 (1965).